Supplementary Materials

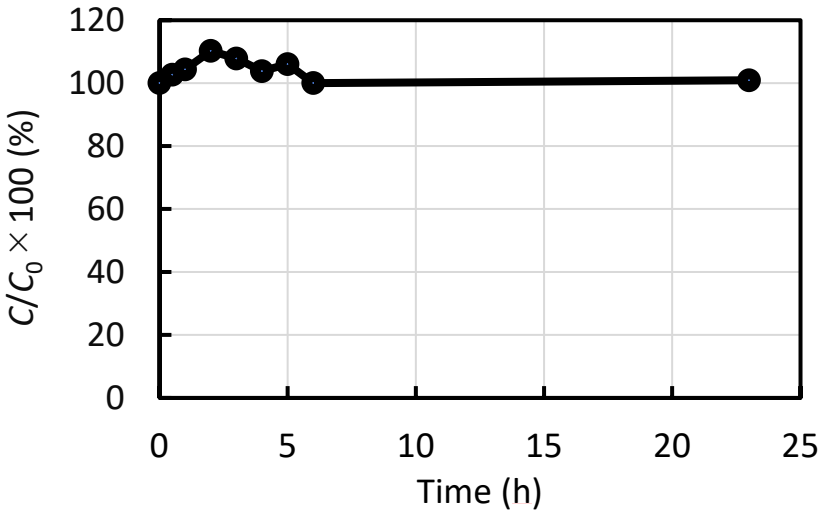

Figure S1. Time profile of concentration ratio ($C/C_0 \times 100\%$) where C and C_0 are concentration of (*S*)-PhEA at each reaction time and 0 h, respectively during the photohydrogenation of **2a** to **2b**. Concentrations of (*S*)-PhEA were determined using the reverse-phase HPLC system as described in the Section 2.2. A mobile phase was methanol/water (2/1) with a flow rate of 0.7 mL/min. Chromatograms were monitored at 230 nm.

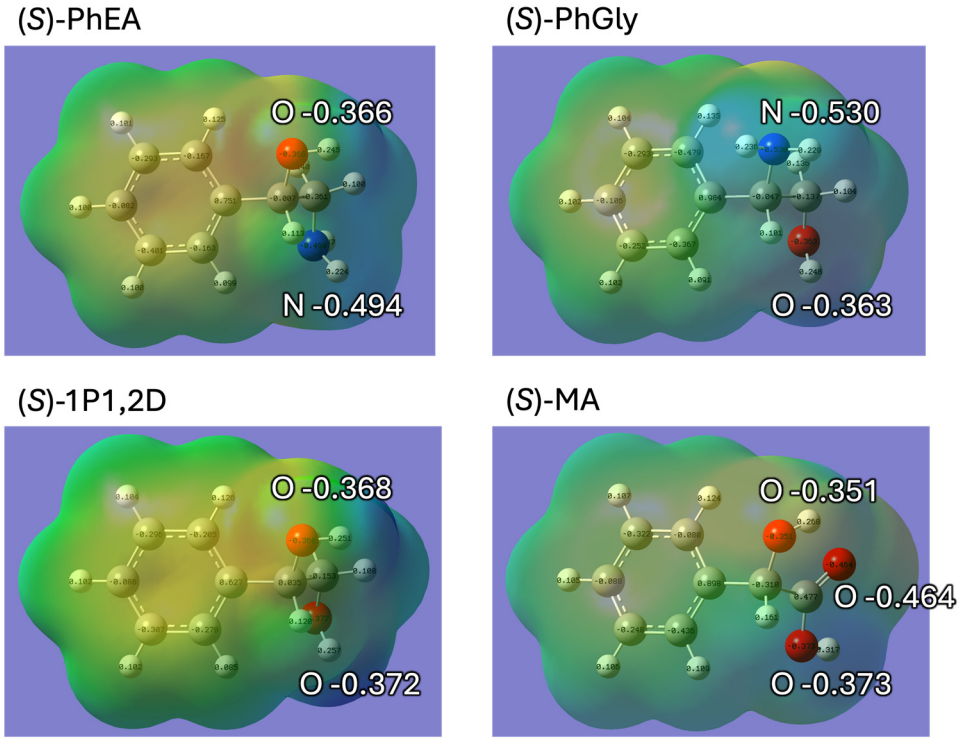

Figure S2. Optimized molecular structures and calculated charge distributions of four chiral co-adsorbents obtained by density functional theory (DFT) calculations using the Gaussian program. Geometry optimizations were performed for the ground-state structures using the APFD functional with the default spin multiplicity. The 6-311+G(2d,p) basis set was employed for all atoms.

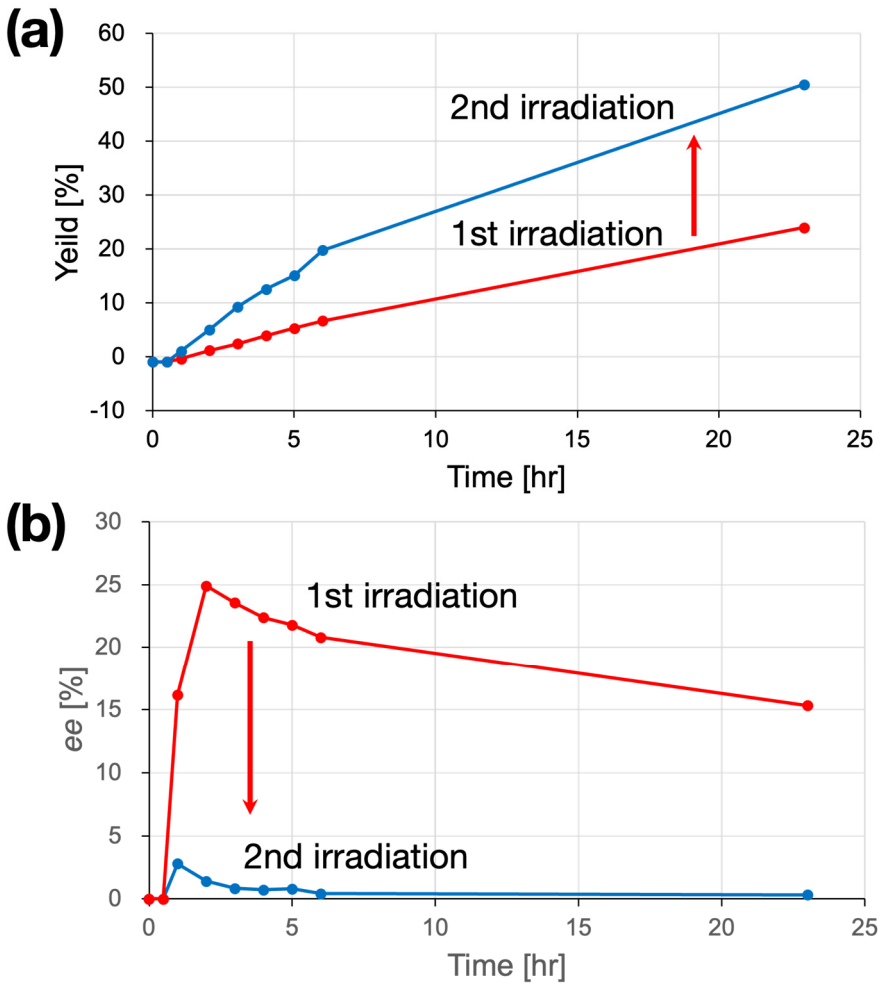

Figure S3. Time courses of (**a**) yield and (**b**) enantiomeric excess (*ee*) during two consecutive enantioselective photohydrogenation experiments. Reaction conditions: TiO_2 (TIO-13), substrate (2NP), and chiral co-adsorbent ((*S*)-PhEA).

Table S1. Comparison of yield, *ee*, and inhibition ratio (*IR*) between a single experiment and repeated experiments (1st and 2nd irradiations). Reaction conditions: TiO_2 (TIO-13), substrate (2NP), and chiral co-adsorbent ((*S*)-PhEA).

		Yield (%)	%*ee*	*IR* (%)
Single run		35	–20(*S*)	86
Repeated experiment	1st	24	–15(*S*)	82
	2nd	51	–0.3(*S*)	51

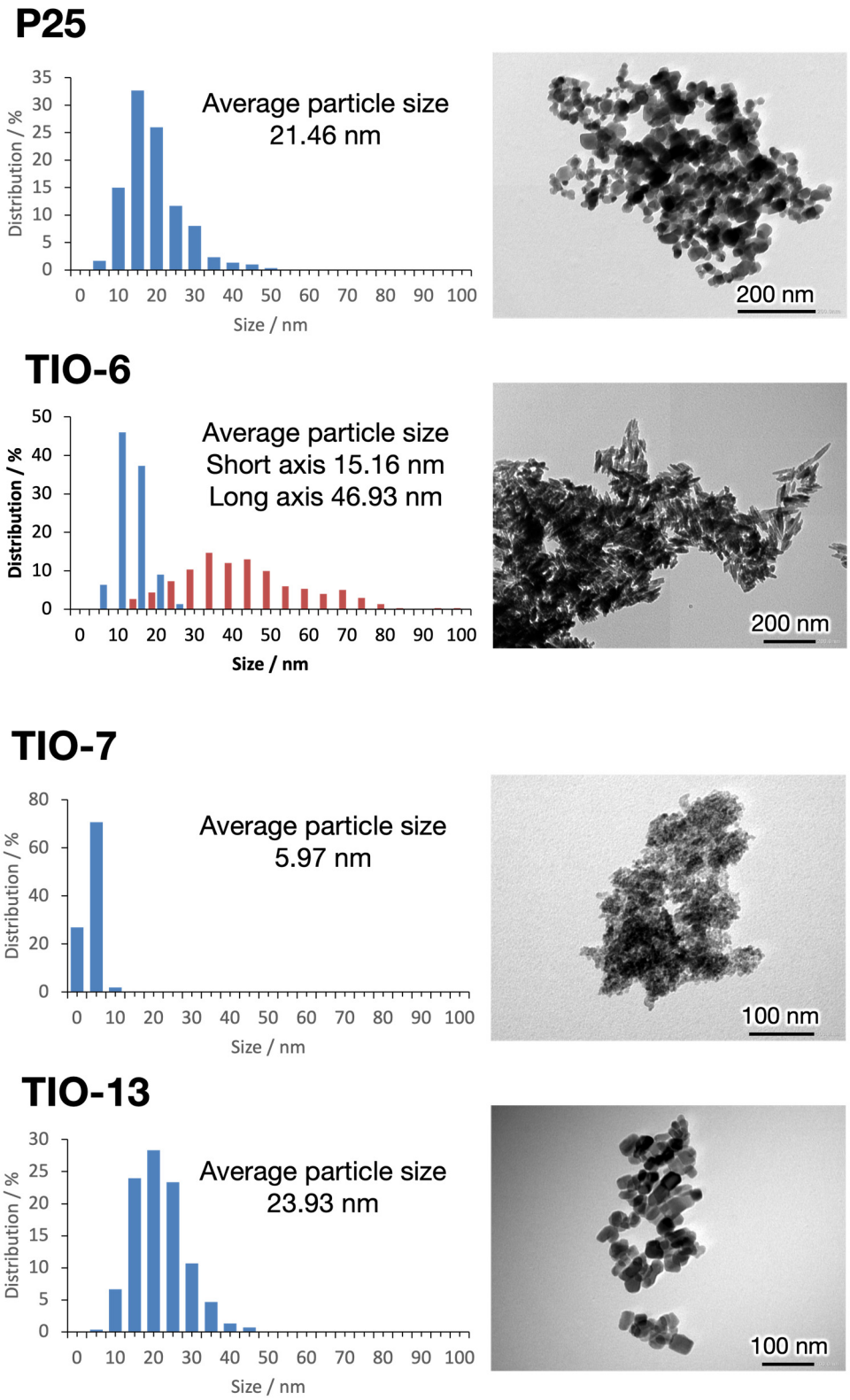

Figure S4. TEM images and corresponding particle size distributions of four TiO_2 samples. Representative TEM images of P25, TIO-6, TIO-7, and TIO-13 are shown together with the particle size distributions obtained by statistical analysis of the TEM images. Particle diameters were measured directly from the TEM images by counting approximately 300 particles for each sample. For rutile TIO-6, particle sizes were evaluated along both the long and short axes due to its anisotropic rod-like morphology.

Table S2. XRD data for anatase TiO_2 samples TIO-13 and TIO-7. The table lists the diffraction angles (2θ), corresponding Miller indices (hkl), peak intensities, and integrated peak areas for each sample. To facilitate comparison of crystal morphology and preferentially exposed facets, the ratios of the integrated peak areas relative to that of the {200} reflection (S_{hkl}/S_{200}) are also included. The black bold outline indicates the reference area ratio of the {200} reflection ($S_{200}/S_{200} \times 100 = 100\%$), while the red bold outlines indicate the area ratios of the {004} and {220} reflections relative to the {200} reflection (S_{004}/S_{200} and S_{220}/S_{200}), which are discussed and compared in the main text.

			TIO-13			**TIO-7**		
	2θ/degree	***h,k,l***	**Peak Intensity**	**Area**	**S_{hkl}/S_{200}**	**Peak Intensity**	**Area**	**S_{hkl}/S_{200}**
1	25.3	1,0,1	5916	101.5	340.53	1927	74.3	351.69
2	37.0	1,0,3	399	5.9	19.75	86	6.3	29.64
3	37.8	0,0,4	1195	20.4	68.42	351	11.5	54.66
4	38.6	1,1,2	441	6.7	22.62	102	7.2	34.16
5	48.0	2,0,0	1568	29.8	100.00	483	21.1	100.00
6	53.9	1,0,5	1000	18.9	63.53	290	11.6	54.86
7	55.1	2,1,1	976	18.8	62.95	282	12.7	59.92
8	62.1	2,1,3	173	3.1	10.39	22	4.9	23.25
9	62.7	2,0,4	726	14.3	47.83	206	7.2	33.91
10	68.8	1,1,6	331	6.3	21.04	73	3.1	14.77
11	70.3	2,2,0	355	7.0	23.55	83	4.1	19.60

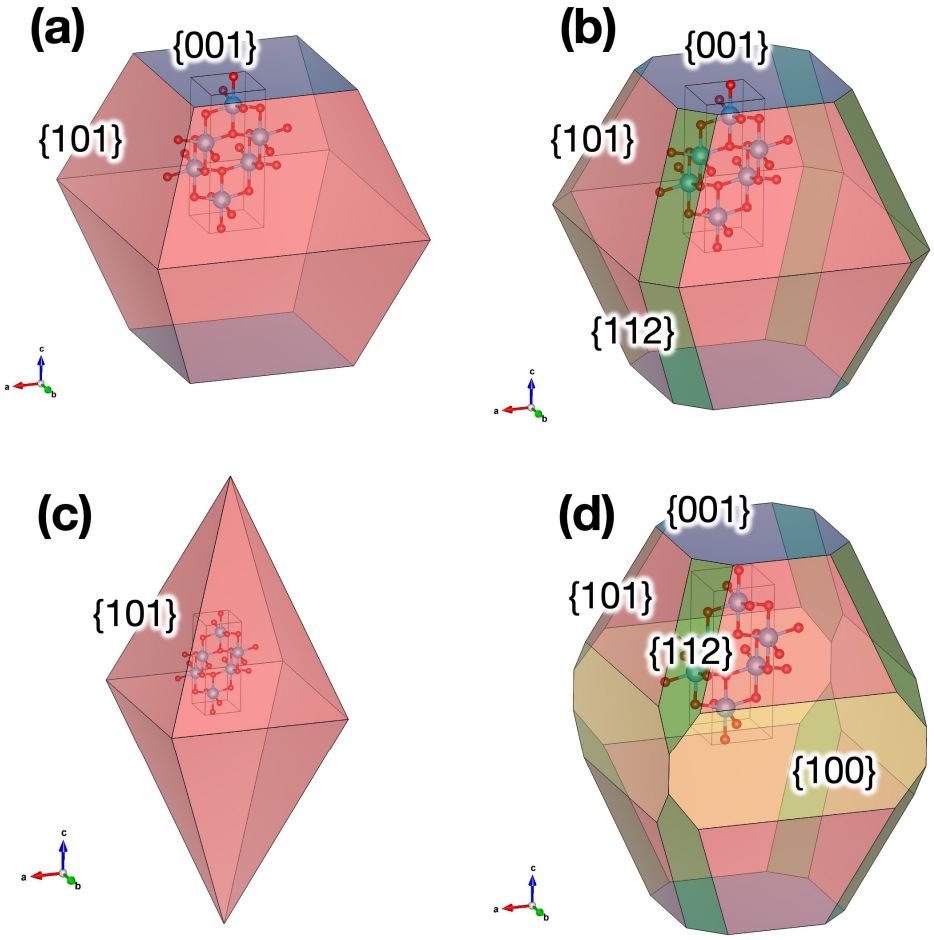

Figure S5. Schematic illustrations of representative anatase TiO_2 particle morphologies and exposed crystal facets discussed in this study. Visualizations were performed with the VESTA program. (**a**) A decahedral-like morphology exposing predominantly {101} facets with minor {001} facets, which is considered to represent the crystal shape formed by TIO-13. (**b**) A distorted morphology with reduced edges and partial exposure of {112} facets, which is proposed for TIO-7 as a consequence of smaller particle size and lattice distortion. (**c**) An octahedral morphology without {001} facets, shown for reference as a model exposing only {101} facets. (**d**) A further truncated morphology derived from (**b**), in which additional reduction of edges leads to partial exposure of {100} facets, illustrating a possible highly distorted surface structure. In all schematics, the exposed crystal facets are color-coded as follows: red, {101}; blue, {001}; green, {112}; and yellow, {100}. These schematic models are intended to provide a conceptual visualization of the differences in surface structure and facet heterogeneity discussed in Sections 3.3 and 3.4, rather than exact atomic-scale representations.

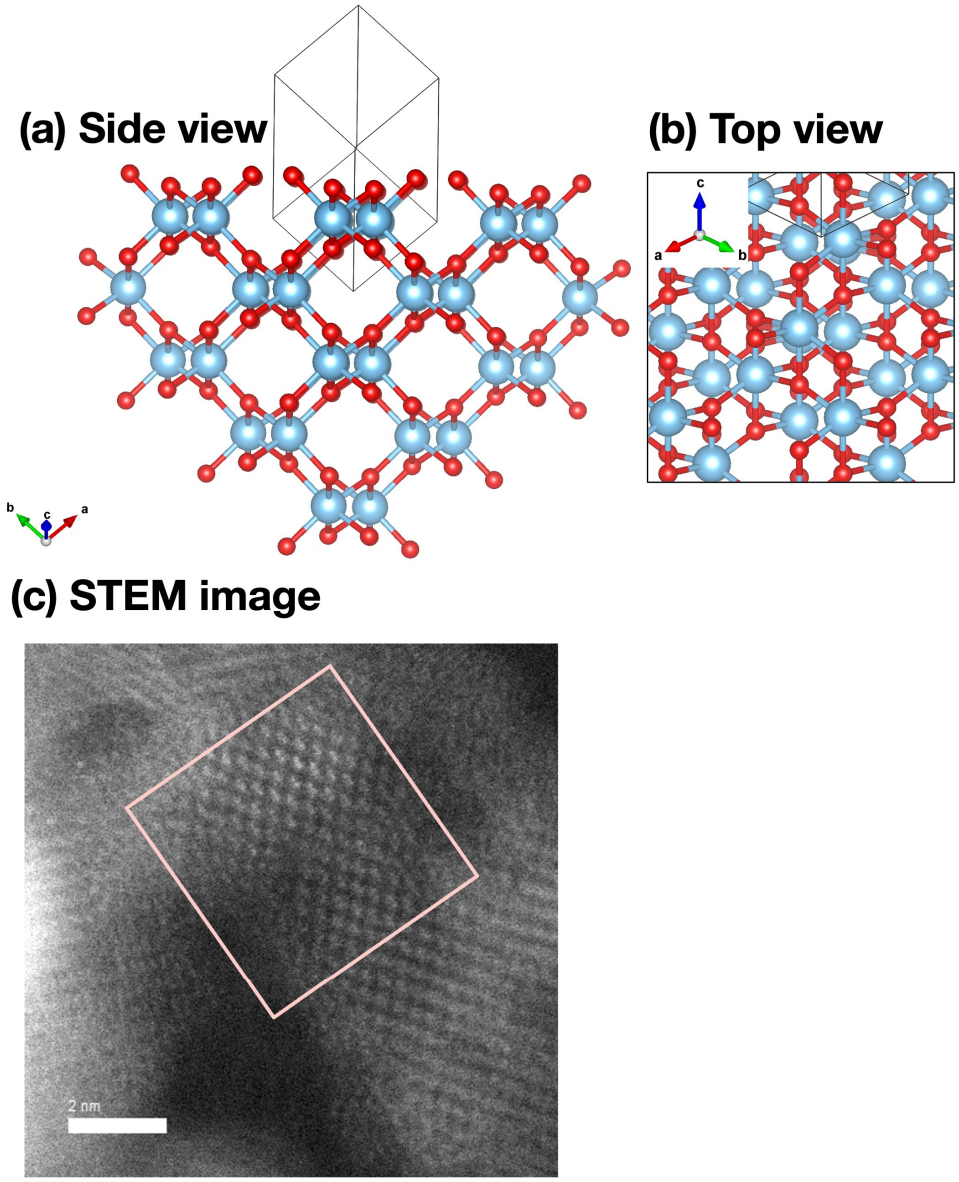

Figure S6. Bulk-cut atomic models, top-view representations, and corresponding STEM observations of the anatase TiO_2 (112) surface. Visualizations were performed with the VESTA program. (**a**) Side-view atomic geometry of the bulk-cut anatase (112) surface model, illustrating the characteristic stepped surface structure. (**b**) Top-view representation of the same (112) surface, highlighting the arrangement of surface Ti and O atoms characteristic of this high-index facet. (**c**) Representative STEM image showing lattice fringes and atomic arrangements corresponding to a side-view projection of the anatase (112) surface, as observed for TIO-7. The bulk-cut models in (**a**,**b**) represent idealized surface geometries derived from the anatase bulk structure and are intended for qualitative comparison with the experimental STEM observations in (**c**).

Table S3. Comparison of initial reaction rates (mmol·L^{-1}·hr^{-1}) for the photohydrogenation of substrates **1a** (1NP) and **2a** (2NP) over four TiO_2 photocatalysts. The initial rates were measured in the absence of a chiral co-adsorbent and in the presence of MA or PhEA as chiral co-adsorbents. For each substrate–co-adsorbent combination, data for the *S*-enantiomer are shown in the upper rows (S) and those for the *R*-enantiomer in the lower rows (R). The time intervals used for deriving the initial reaction rates depended on the presence of the co-adsorbent and the corresponding inhibition behavior: 23 h for MA, 5 h for PhEA, and 3 h in the absence of a co-adsorbent. These time windows were selected to ensure linearity of product formation under each condition.

Initial Reaction Rates [mmol·L^{-1}·hr^{-1}]		**TiO_2 Powder**			
Substrate	**Chiral Co-Adsorbents**	**P25**	**TIO-13**	**TIO-7**	**TIO-6**
1 a 1NP	MA [a]	S: 0.0016 R: 0.0027	S: 0.0006 R: 0.0039	S: 0.0234 R: 0.0233	S: 0.0032 R: 0.0040
	PhEA [b]	S: 0.0696 R: 0.0527	S: 0.0149 R: 0.0067	S: 0.0419 R: 0.0340	S: 0.0673 R: 0.0612
	none [c]	S: 0.6728 R: 0.6678	S: 0.0864 R: 0.0843	S: 0.2018 R: 0.1929	S: 0.2018 R: 0.1929
2 a 2NP	MA [a]	S: 0.0041 R: 0.0047	S: 0.0017 R: 0.0019	S: 0.0652 R: 0.0609	S: 0.0030 R: 0.0034
	PhEA [b]	S: 0.1124 R: 0.0918	S: 0.0383 R: 0.0207	S: 0.0713 R: 0.0525	S: 0.0700 R: 0.0665
	none [c]	S: 0.7439 R: 0.7424	S: 0.1655 R: 0.1647	S: 0.3086 R: 0.3076	S: 0.3630 R: 0.3612

[a] Initial reaction rates during 0–23 h irradiation. [b] Initial reaction rates during 0–5 h irradiation. [c] Initial reaction rates during 0–3 h irradiation.